Effects of Prandtl number on the laminar cross flow past a heated cylinder

S. Ajith Kumar, Manikandan Mathur, A. Sameen, and S. Anil Lal

Effects of Prandtl number on the laminar cross flow past a heated cylinder

S. Ajith Kumar,[1] Manikandan Mathur,[1] A. Sameen,[1,a] and S. Anil Lal[2]

[1]*Department of Aerospace Engineering, Indian Institute of Technology Madras, Chennai 600036, India*
[2]*Department of Mechanical Engineering, College of Engineering Trivandrum, Trivandrum, Kerala, India*

Flow past a heated cylinder at constant surface temperature is computationally simulated and analyzed in the laminar regime at moderate buoyancy. The parameters governing the flow dynamics are the Reynolds number, Re, the Richardson number, Ri, and the Prandtl number, Pr. We perform our computations in the range $10 \leq Re \leq 35$, for which the flow past an unheated cylinder results in a steady separation bubble, and vary the other two parameters in the range $0 \leq Ri \leq 2$, $0.25 \leq Pr \leq 100$. The heat transfer from the entire cylinder surface, quantified by the average Nusselt number Nu_{avg}, is shown to obey $Nu_{avg} = 0.7435 Re^{0.44} Pr^{0.346}$ in the mixed convection regime we investigate. For a fixed Re and Pr, the flow downstream of the cylinder becomes asymmetric as Ri is increased from zero, followed by a complete disappearance of the vortices in the recirculation bubble beyond a threshold value of Ri. For a fixed Re and Ri, the vortices in the recirculation bubble are again observed to disappear beyond a threshold Pr, but with the reappearance of both the vortices above a larger threshold of Pr. In the limit of large Pr, the time-averaged flow outside the thermal boundary layer but within the near-wake region regains symmetry about the centerline and ultimately converges to a flow field similar to that of $Ri = 0$; in the far-wake region, however, we observe asymmetric vortex shedding for moderate Pr. The thermal plume structure in the cylinder wake is then discussed, and the plume generation is identified at points on the cylinder where the Nusselt number is a local minimum. The difference between the plume generation and the flow separation locations on the cylinder is shown to converge to zero in the limit of large Pr. We conclude by plotting the lift and drag coefficients as a function of Ri and Pr, observing that C_D decreases with Ri for $Pr < Pr_t$ (and vice versa for $Pr > Pr_t$), where $Pr_t \approx 7.5$. *Published by AIP Publishing.* [http://dx.doi.org/10.1063/1.4966937]

I. INTRODUCTION

Flow past a cylinder and the associated wake dynamics are fundamentally interesting and important in engineering. Extensive literature on external flows is currently available, especially on the flow past a circular cylinder,[1–7] investigating a plethora of issues like the aerodynamic forces, boundary layer phenomena, vortex induced vibrations, and the transition to turbulence. In this paper, we investigate the flow past a heated cylinder, a scenario relevant for a wide variety of engineering applications such as heat exchangers, chimney stacks, and hot wire anemometers. Specifically, we focus on the effects of Prandtl number (defined as the ratio between the kinematic viscosity and the thermal diffusivity of the fluid), in the presence of buoyancy force, on the steady, asymmetric wake bubble that forms in the flow past a heated cylinder. Most earlier studies on the flow past a heated cylinder are based on the assumption that buoyancy is negligible, i.e., the

a)sameen@ae.iitm.ac.in

Richardson number Ri, defined as the ratio of the buoyancy force to the inertia force, is either close to or equal to zero.[8–11] For example, the widely used King's law for the calibration of hot wire anemometers assumes negligible buoyancy. Flow control strategies that use heating or cooling a surface also assume negligible buoyancy.[8] The literature discussed here, however, pertains mostly to the work which included buoyancy force in the analysis.

Studies on thermal convection flows with finite Ri have been pioneered by Gebhart *et al.*[12] and Gebhart and Pera.[13] An experimental study by Oosthuizen and Madan[14] on the vortex shedding regime of air flow past a heated cylinder in various configurations (such as horizontal cylinder, and vertical cylinder) concluded that pure forced convection occurs for $Ri < 0.53$. Fand and Keswani[15] performed further experiments in water (again in the vortex shedding regime) to classify the flow past a heated cylinder into four regimes based on the nature of convection occurring on the cylinder surface. The regimes, in terms of the Richardson number Ri, are as follows: (1) $Ri < 0.5$: pure forced convection, (2) $0.5 < Ri < 2$: forced convection dominates natural convection, (3) $2 < Ri < 40$: natural convection dominates forced convection, and (4) $Ri > 40$: pure natural convection. Vilimpoq *et al.*[16] found that the Prandtl number of the fluid shifts the demarcation of these regimes dramatically. Co-existence of the viscous and thermal boundary layers and their mutual interaction are so critical that it leads to a migration of the different flow regimes to larger or smaller values of Ri at different values of Pr.

Most studies that include cylinder surface heating perform their investigations in the unsteady, vortex-shedding regime. Various experimental and computational studies at values of Re well above 50 ($Re \approx 47$ is when vortex shedding is initiated in the flow past an unheated cylinder) have highlighted the role of the Richardson number in the asymmetry that occurs between the upper and lower shed vortices upon heating the cylinder.[17–19] The effects of Prandtl number variation are, however, not discussed in these studies where the Richardson number is finite. On the other hand, the effects of Prandtl number on the forced convection regime, i.e., in the limit of $Ri = 0$ and Re again being well above 50, have been previously discussed,[20–22] identifying Re and Pr as the influencing factors for the average Nusselt number, Nu_{avg}. In this paper, we focus on the Prandtl number effects in the steady regime, i.e., Re well below 47 and values of Ri that extend from the forced to mixed convection regimes.

The values of Pr and Ri that are considered in the existing literature are shown in Table I, where only those studies with $Re \lesssim 100$ are shown. One of the earliest experiments to come up with a heat transfer correlation with Re was performed by Collis and Williams.[8] The resulting Nusselt number expression as a power law in terms of Re is, however, valid only in the forced convection regime as is the case in the numerical studies of Dennis and Chang[3] and Dennis *et al.*[10] Other numerical studies[9] assumed zero buoyancy too, performing investigations at a fixed Prandtl number of 0.72. Lange *et al.*[26] included property variation due to the temperature in their computation of crossflow past a heated cylinder of micron sized diameter. Wang *et al.*[27] Wang and Travnicek[28] suggested a new representation of temperature called effective temperature while discussing a heat transfer correlation, with both the studies being for a fixed $Pr = 0.7$. Biswas and Sarkar[32] computed the flow past a heated cylinder at low Re and fixed Pr with free slip boundary conditions at the top and bottom boundaries of the computational domain. The free slip boundary conditions resulted in a recirculating bubble at the top boundary in the presence of buoyancy.

In the list of studies shown in Table I, Prandtl number variation is considered only by Refs. 10, 16, and 31. The studies by Dennis *et al.*[10] and Bharti *et al.*,[31] however, assume that there is no coupling between the momentum and energy equations, i.e., $Ri = 0$. The flow as well as the heat transfer behavior in this forced convection regime ($Ri = 0$) cannot be simply extended to the regime of mixed convection, adding to the motivation for our studies presented in this paper. The experimental study by Vilimpoq *et al.*[16] does present results for $Ri > 0$ and varying Pr.

Vilimpoq *et al.*[16] performed holographic interferometry measurements to obtain the isotherms and consequently quantify the Nusselt number variation on the cylinder surface. Based on their empirical data, they obtain a correlation that describes the variation of the average Nusselt number as a function of the Reynolds and Prandtl numbers in the range $5 \leq Re \leq 64$ and $Ri \leq 0.5$, estimating that 90% of the experimental data fall within 10% of the estimated correlation. In the present paper, we perform a quantitative comparison of the Nusselt number distribution with the

TABLE I. The range of values of *Re*, *Ri*, and *Pr* considered in the earlier studies on the flow past a heated circular cylinder in cross flow (free stream flow direction orthogonal to the buoyancy force direction). "Comp." and "Expt." refer to computational and experimental studies, respectively. Dash indicates missing parameters in the original reference.

Reference	*Re*	*Ri*	*Pr*	Comp./Expt.
Collis and Williams[8]	0.01-140	...	0.71	Expt.
Acrivos *et al*.[23]	25-180	0	0.71	Expt.
Dennis *et al*.[10]	0.01-40	0	$0.73-2^{15a}$	Comp.
Dennis and Chang[3]	5-100	0	...	Comp.
Fand and Keswani[15]	$0-160^a$	$0-40$	7	Expt.
Lee *et al*.[24]	5-100	0-4	0.72	Comp.
Jafroudi and Yang[9]	1-40	...	0.72	Comp.
Vilimpoq *et al*.[16]	0.002-64	0.001-4.4	5.5-27 000	Expt.
Dumouchel *et al*.[25]	30-120	<0.12	0.7^a	Expt.
Lange *et al*.[26]	10^{-4}-200	0^a	0.7	Comp.
Wang *et al*.[27]	$50-160^a$	<0.02	0.71	Expt.
Wang and Travnicek[28]	5-163	<5	0.7	Expt.
Shi *et al*.[29]	0.001-170	...	0.714	Comp.
Wu *et al*.[30]	<280	0	...	Both
Bharti *et al*.[31]	10-45	0	0.7-400	Comp.
Biswas and Sarkar[32]	10-45	1-2	0.7	Comp.
Sen *et al*.[7]	6-40	0	0.71	Comp.
Present	**≤35**	**0-2**	**0.25-100**	**Comp.**

[a]Indicates inferred values from the original papers. The boldface values indicate the present work.

experimental results of Vilimpoq *et al*.[16] for specific values of the parameters, and proceed to perform a more detailed systematic study of the isotherms for various *Ri* and *Pr*. We also estimate a more accurate correlation for the average Nusselt number that is valid over a wider range of *Ri*. Furthermore, to the best of our knowledge, no previous study has investigated the dependence of the wake structure, flow pattern, and the aerodynamic force coefficients as a function of the Prandtl number for *Ri* > 0.

In this paper, the effects of Prandtl number in the low Reynolds number (*Re* ≤ 35) regime, where the flow past an unheated cylinder is steady, are discussed for cases with non-zero *Ri*. The numerical formulation is described in Section II. The variation of the Nusselt number as a function of *Re*, *Pr*, and *Ri* is discussed in Section III A. The dramatic changes in the wake behind the cylinder with a change in the Prandtl number are discussed in Section III B. Plume generation, flow separation, and the corresponding consequences for the heat transfer are discussed in Section III C. We investigate the variation of the aerodynamic force coefficients in Section III D, followed by a summary of all the results and the corresponding conclusions in Section IV.

II. NUMERICAL FORMULATION

The incompressible mass conservation, Navier-Stokes, and energy equations in a two-dimensional Cartesian co-ordinate system form the governing equations of the flow. The buoyancy-driven flow from a heated cylindrical surface, whose temperature is held constant, interacts with the laminar mean flow to yield mixed convection conditions. The dimensionless forms of the conservation equations for mass, momentum, and energy with the Boussinesq approximation are

$$\frac{\partial u}{\partial x} + \frac{\partial v}{\partial y} = 0, \tag{1}$$

$$\frac{\partial u}{\partial t} + u\frac{\partial u}{\partial x} + v\frac{\partial u}{\partial y} = -\frac{\partial p}{\partial x} + \frac{1}{Re}\left(\frac{\partial^2 u}{\partial x^2} + \frac{\partial^2 u}{\partial y^2}\right), \tag{2}$$

$$\frac{\partial v}{\partial t} + u\frac{\partial v}{\partial x} + v\frac{\partial v}{\partial y} = -\frac{\partial p}{\partial y} + \frac{1}{Re}\left(\frac{\partial^2 v}{\partial x^2} + \frac{\partial^2 v}{\partial y^2}\right) + RiT, \tag{3}$$

$$\frac{\partial T}{\partial t} + u\frac{\partial T}{\partial x} + v\frac{\partial T}{\partial y} = \frac{1}{RePr}\left(\frac{\partial^2 T}{\partial x^2} + \frac{\partial^2 T}{\partial y^2}\right). \tag{4}$$

The non-dimensional horizontal and vertical spatial coordinates x and y are obtained using the cylinder diameter D as the length scale. The corresponding non-dimensional velocity components u and v are obtained using the horizontal free stream velocity U_0 as the velocity scale. The non-dimensional temperature T is defined as $T = (T_d - T_0)/(T_w - T_0)$, where T_d is the dimensional temperature, T_0 the constant free stream temperature, and T_w the constant cylinder wall temperature. The pressure is non-dimensionalized with $\rho_0 U_0^2$ to obtain p, with ρ_0 being the fluid density at temperature T_0. The non-dimensional numbers appearing in Equations (2)-(4) are the Reynolds number Re, the Richardson number Ri, and the Prandtl number Pr, defined as

$$Re = \frac{U_0 D}{\nu}, \tag{5}$$

$$Ri = \frac{Gr}{Re^2} = \frac{\beta g \Delta T_d D}{U_0^2}, \tag{6}$$

where $Gr = \beta g \Delta T_d D^3/\nu^2$ is the Grashof number, and

$$Pr = \frac{\nu}{\kappa}, \tag{7}$$

with g being the acceleration due to gravity. The fluid properties are described by the thermal diffusivity κ, the kinematic viscosity ν, and the thermal expansion coefficient β, all of which are assumed to be constants. The dimensional temperature difference between the cylinder wall and the freestream is given by $\Delta T_d = T_w - T_0$. In this paper, $Ri = 0$ is interpreted as zero buoyancy.

The boundary conditions for solving Equations (1)-(4) are shown in Figure 1 and described as follows. The non-dimensional velocity components at the inlet ($x = -4.5$, chosen based on the domain independence study discussed later in this section) of the computational domain are $u = 1.0$, $v = 0.0$. The temperature boundary conditions are $T = 0$ at $x = -4.5$ and $T = 1$ on the cylinder surface. No-slip and no-normal-flow boundary conditions are imposed on the cylinder wall, i.e., $u = v = 0$ at the cylinder surface. The bottom ($y = -4.5$) and top ($y = 4.5$) boundaries are subjected to stress-free conditions, i.e., $\partial u/\partial y = \partial v/\partial y = \partial T/\partial y = 0$. The boundary conditions on the right boundary at $x = 30$ are $\partial u/\partial x = \partial v/\partial x = \partial T/\partial x = 0$.

The governing Equations (1)-(4) in primitive variables (u, v, p, T) are nonlinear coupled partial differential equations. A projection method is employed for decoupling velocity and pressure. Projection methods are fractional step methods based on the decomposition of velocity field into an intermediate velocity field and the gradient of a scalar field.[33] Fractional step methods integrate the Navier-Stokes equations in time; at each time step, the momentum equation is solved without considering the pressure field to yield an intermediate velocity field that does not satisfy the continuity equation. The pressure Poisson equation is discretized on the control volumes using a central difference scheme. The divergent free velocity components are then obtained by correcting the intermediate velocity using the gradient of pressure.
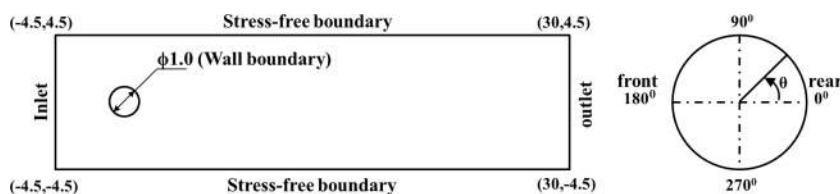
FIG. 1. A schematic representation of the computational domain and the its boundaries. The cylinder center is at $(x, y) = (0, 0)$.

The computational domain is divided into quadrilateral cells. Each quadrilateral cell is then divided into two linear triangles and the momentum equations are discretized using the standard Galerkin finite element method on the triangular elements. The velocity components are explicitly evaluated at the nodes of the triangles using the projection method discussed above. The pressure Poisson equation is discretized on each quadrilateral cell using a cell centered finite volume method in which the variation of pressure between nodes is assumed piece-wise linear. The resulting set of simultaneous equations are solved iteratively using the conjugate gradient method to get pressure values at the geometrical centres of the quadrilaterals. Since the velocity components and pressure are evaluated at different points of an element, this approach takes advantage of a staggered grid approach in obtaining stable pressure fields without spurious checkerboard oscillations.[34] The fully explicit method for time integration is subjected to the Courant-Friedrichs-Lewy stability criterion. The computation is continued till the L_2 norms of errors of u, v, and T at a time step m, given by

$$\left[\frac{\sum\limits_{i=0}^{N} \left(\phi_i^m - \phi_i^{m-1} \right)^2}{\sum\limits_{i=0}^{N} \left(\phi_i^m \right)^2} \right]^{1/2}, \tag{8}$$

and is reduced below 10^{-6}, with ϕ denoting u, v, or T and N the total number of nodes used in the computation. This criterion for convergence is strictly valid only for steady flows, and we therefore check the temporal evolution of other integral quantities such as the lift and drag coefficients, and the average Nusselt number for flows that converge to an unsteady, oscillatory state. This hybrid finite element-finite volume code has been tested satisfactorily on a number of benchmark problems such as the flow in a lid-driven square cavity, the steady and unsteady regimes in the uniform flow past an unheated circular cylinder, flow in a backward facing step and the natural convection flow in a temperature-driven cavity.[34]

The length and height of the computational domain are selected based on four case studies for which the Strouhal number ($St = fD/v$, where f is the vortex shedding frequency), the lift coefficient C_L (defined in Equation (9)), and the average Nusselt number (defined in Equation (12)) are compared, as shown in Table II. The time-averaging (denoted by $\langle \cdot \rangle$) for each case is performed over exactly one period of oscillations, which is determined by plotting C_L as a function of time. The aerodynamic force coefficients C_L and C_D are computed as

$$C_L = \int_0^{2\pi} \left(-p \sin\theta + \frac{1}{Re} \frac{\partial u_\theta}{\partial r} \cos\theta \right) d\theta, \tag{9}$$

$$C_D = \int_0^{2\pi} \left(-p \cos\theta - \frac{1}{Re} \frac{\partial u_\theta}{\partial r} \sin\theta \right) d\theta, \tag{10}$$

where the integral is evaluated on the cylinder surface, and the azimuthal component of velocity is given by $u_\theta = -u \sin\theta + v \cos\theta$. The comparative study tabulated in Table II for $Re = 100$, $Ri = 1$, $Pr = 0.7$ shows that the results are independent of the domain size for domains larger than $34.5D \times 9D$. Indeed, we have verified this domain independence for larger values of Pr also. Figure 1 shows the dimensions of the rectangular computational domain selected for the analyses presented in the rest of this paper. In Table III, we present the results corresponding to four different grids with different number of elements. Based on the computed values of C_L, St, and Nu_{avg} (defined

TABLE II. Comparison of various time-averaged (indicated by $\langle \cdot \rangle$) quantities for different domain sizes (Re = 100, Ri = 1.0, and Pr = 0.7).

Length	Height	Elements	Nodes	St	$\langle C_L \rangle$	$\langle Nu_{avg} \rangle$	$(C_L - \langle C_L \rangle)^{rms}$	$(Nu_{avg} - \langle Nu_{avg} \rangle)^{rms}$
32.5D	7D	36 300	36 640	0.192	−1.283	5.320	0.0012	0.0018
34.5D	9D	50 000	50 575	0.191	−1.272	5.385	0.0012	0.0016
36.5D	11D	65 200	66 044	0.191	−1.272	5.387	0.0011	0.0015
38.5D	13D	80 200	81 314	0.191	−1.272	5.387	0.001	0.0015

TABLE III. Grid sensitivity study for various time-averaged (indicated by $\langle \cdot \rangle$) quantities (Re = 100, Ri = 1.0, and Pr = 0.7) for a fixed domain size of $34.5D \times 9D$.

Elements	$\langle C_L \rangle$	St	$\langle Nu_{avg} \rangle$
34 896	−1.294	0.189	5.216
50 000	−1.272	0.191	5.385
75 024	−1.275	0.192	5.386
100 236	−1.276	0.192	5.385

in Equation (12)) for $Re = 100$, $Ri = 1$, and $Pr = 0.7$ using various grid resolutions, we choose to represent the full domain using 50 000 elements for all the results presented in the rest of this paper. As shown in Table IV, we also confirmed that the domain with 50 000 elements is sufficiently fine to describe the large Pr flows as well. For all the computations, we ensured that there are at least 8 grid points within both the viscous and the thermal boundary layers.

The heat transfer occurring at the cylinder surface is best described using the relative magnitudes of convection and conduction, quantified by the Nusselt number. The Nusselt number Nu is defined as in the work of Verzicco and Camussi,[35]

$$Nu_\theta = -\frac{\partial T}{\partial r}\bigg|_{r=1/2}, \tag{11}$$

where $r = \sqrt{x^2 + y^2} = 1/2$ denotes the cylinder surface and the subscript θ being the polar angle measured from the rear point of the cylinder in the anticlockwise direction, as shown in Figure 1. The average Nusselt number Nu_{avg} is obtained by integrating Nu_θ around the entire cylinder surface,

$$Nu_{avg} = \frac{1}{2\pi} \int_0^{2\pi} Nu_\theta d\theta. \tag{12}$$

The average Nusselt number Nu_{avg} for $Ri = 0$, $Pr = 0.7$, and various Re is compared with the values in the existing literature, as shown in Table V.

It is noteworthy that the various references in Table V implement different boundary conditions on the outer boundaries of the computational domain, but still reasonably agree with our results for the case of $Ri = 0$, i.e., no coupling between the momentum and energy equations. For $Ri > 0$, however, the flow field depends sensitively on the specific boundary conditions implemented on the domain boundaries. We validated our code further by computing the vortex shedding frequency in the flow generated using the boundary conditions of Chatterjee,[38] who implemented no-normal-flow boundary condition ($v = 0$) on the upper and lower boundaries of the domain whose downstream length was $30D$. Specifically, for $Re = 35$, $Ri = 0.9$, and $Pr = 0.7$, Chatterjee[38] report $St = 0.15$, while our code computes a flow with $St = 0.146$. In the rest of this paper, all the results correspond to the boundary conditions described earlier (and shown in Figure 1) in this section, to simulate flows in unbounded domains. In the rest of the paper, we choose to not include the notation $\langle \cdot \rangle$ in Nu_θ, Nu_{avg}, C_L, and C_D since the temporal variations in these quantities are negligible in the regimes we study.

TABLE IV. Grid sensitivity study for various time-averaged (indicated by $\langle \cdot \rangle$) quantities (Re = 25, Ri = 1.0, and Pr = 100) for a fixed domain size of $34.5D \times 9D$.

Elements	$\langle C_L \rangle$	$\langle C_D \rangle$	$\langle Nu_{avg} \rangle$
34 896	0.37	2.14	14.56
50 000	0.39	2.18	14.74
75 024	0.39	2.18	14.74
100 236	0.39	2.18	14.74

TABLE V. Comparison of Nu_{avg} from the present computations with the results from the existing literature (the computational schemes used in each of the references are indicated within brackets) for $Ri = 0$ and $Pr = 0.7$.

Literature	$Re = 10$	$Re = 20$	$Re = 40$
Dennis *et al*.[10] (2D finite difference)	1.8673	2.5216	3.4317
Lange *et al*.[26] (FVM, simple)	1.8101	2.4087	3.2805
Sparrow *et al*.[36] (expt.)	1.6026	2.2051	3.0821
Soares *et al*.[37] (second-order upwind)	1.8600	2.4300	3.2000
Bharti *et al*.[31] (semi-implicit finite volume)	1.8623	2.4653	3.2825
Present computations (FEM-FVM hybrid)	1.8663	2.5039	3.3723

III. RESULTS AND DISCUSSIONS

Computations are performed for the following range of parameters: $Re \leq 35$, $0 \leq Ri \leq 2$, and $0.25 \leq Pr \leq 100$. We also include some results for $Pr = 1000$ wherever necessary, ensuring that the thermal boundary layer always contains at least eight grid points. We recall that $Re \leq 45$ corresponds to a steady, symmetric wake bubble for $Ri = 0$.[6] Depending on the value of Ri, the flow around the cylinder and the wake develops an asymmetry about the horizontal axis ($y = 0$). We start by discussing the asymmetry in heat transfer in Sec. III A

A. Effects of Prandtl number on heat transfer

Most studies on heat transfer in the flow past a heated cylinder assume negligible buoyancy, in which case the temperature is a passive scalar. The Richardson number Ri, defined in Equation (6), is a measure of the buoyancy force relative to the inertial force. Small values of Ri correspond to a low buoyancy force, whereas at larger Ri, the buoyancy force is comparable to the inertial forces, thus resulting in a coupling between the energy equation (4) and the momentum equation (3) through the buoyancy force acting against gravity.

Figure 2 shows the Nusselt number (Nu_θ) distribution around the cylinder for $Re = 25$ and $Ri = 1.0$ computed at different Prandtl numbers. Nu_θ is found to be maximum at the front stagnation point (given by $\theta = 180°$ in the unheated case $\Delta T_d = 0$) for all Pr, decreases to a minimum value
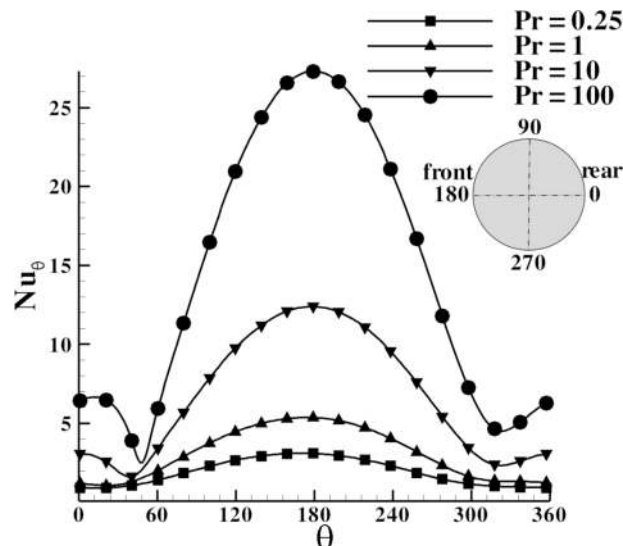
FIG. 2. Nusselt number (Nu_θ) distribution as a function of θ on the surface of the cylinder for $Re = 25$, $Ri = 1.00$, and different values of Pr that are included in the legend.

near the flow separation points on the lower and upper sides of the cylinder, and then increases to a finite value at the rear end of the cylinder ($\theta = 360°$). We note here that the flow separation point and the point where Nu_θ is minimum differ slightly, which we discuss further in detail in Section III C. The increase in Nu_θ upon moving towards the rear of the cylinder from the points of flow separation is attributed to the recirculation bubble behind the cylinder. The flow inside the recirculation bubble continuously transfers heat from the cylinder surface to the fluid, thus increasing Nu_θ. The front stagnation point has a higher Nusselt number compared to the rear as the oncoming fluid is cold ($T = 0$) and hence the temperature gradient normal to the cylinder surface is higher.

We obtain further insights into the Nusselt number variation through temperature contour plots. Figure 3 shows the instantaneous isotherms near the cylinder for various Ri and Pr at $Re = 25$, with the contour values in all the plots being the same. In Figure 3, the isotherms for Ri = 0.25, 1.25, and 1.75 are shown in the left, center, and right columns, respectively. For a fixed Pr, the flow behind the
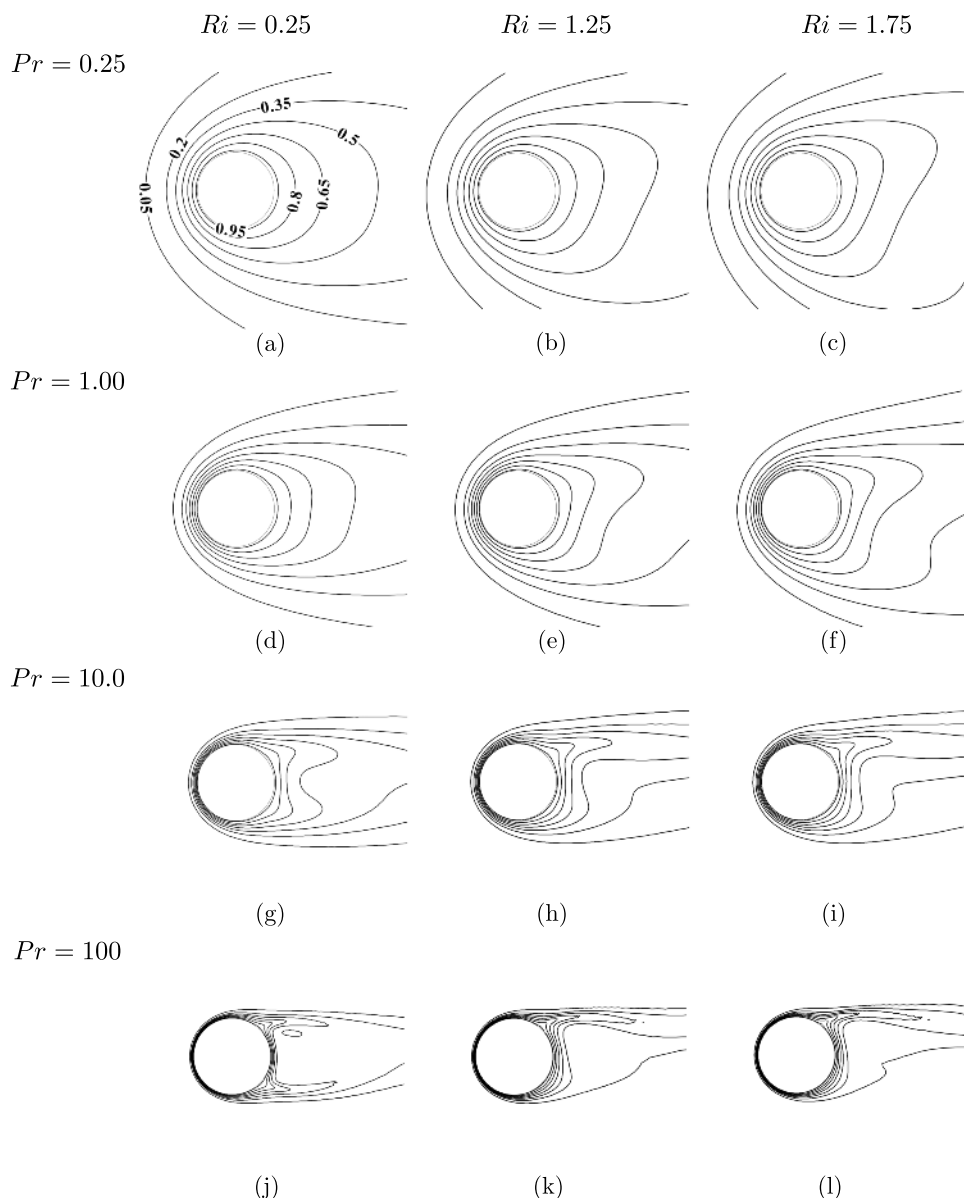
FIG. 3. Instantaneous isotherms for $Re = 25$. Isotherms with the same contour values of T are shown for all the cases. As Pr increases, the thermal boundary layer thickness decreases, while a finite value of Ri introduces an asymmetry in the flow.
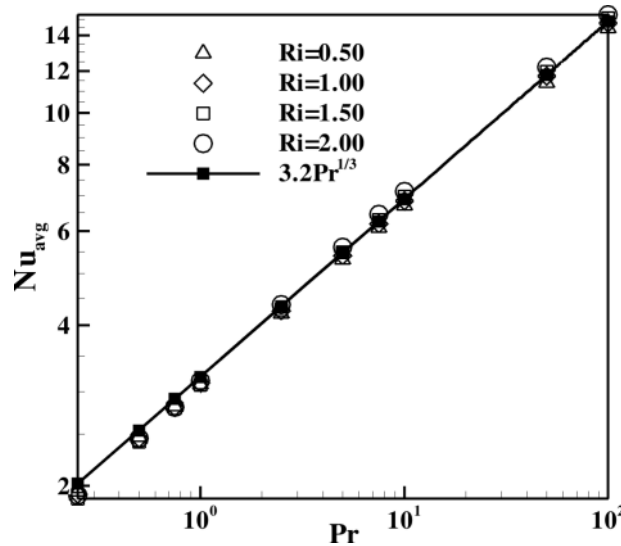
FIG. 4. Variation of Nu_{avg} with Pr for $Re = 25$ and various Ri. A best fit curve obeys $Nu_{avg} = 3.2Pr^{1/3}$.

cylinder shows a clear asymmetry as Ri (or buoyancy) increases. High Pr flows are characterized by small heat diffusion compared to viscous diffusion. As shown in Figure 3, at large Pr the isotherms crowd near the cylinder, thus reducing the thermal boundary layer thickness as compared to small values of Pr. The increase in Nu_θ with Pr shown in Figure 2 is therefore an outcome of the reduced thermal boundary layer thickness or the increase in $\partial T/\partial r$ at the cylinder surface. It is noteworthy that we observe some unsteadiness in the isotherms far from the cylinder for large values of Ri and Pr in Figure 3. This unsteadiness, though present only far from the cylinder surface and hence induces no unsteadiness in the wall-based quantities like Nu, C_L, and C_D, will be discussed in detail in Section III B.

Figure 4 shows the variation of Nu_{avg} (Equation (12)) with Pr for different Ri at $Re = 25$. Nu_{avg} increases with an increase in Pr owing to the decrease in the thermal boundary layer thickness and an increase in the associated temperature gradient on the cylinder surface. At low Pr (≤ 10), Nu_{avg} is insensitive to changes in Ri for the range of Ri considered here ($0.25 \leq Ri \leq 2$). As Pr increases, however, the total heat transfer (or Nu_{avg}) increases slightly with an increase in Ri. The best fit curve in Figure 4 follows $Nu_{avg} = 3.2Pr^{1/3}$ for $Re = 25$. For all other Re for which we ran computations, the exponent is near $1/3$. We now proceed to obtain a correlation similar to the widely used Colburn factor used for the zero buoyancy case ($j = Nu_{avg}/RePr^{1/3}$), by compiling data at different Re.

The Colburn heat transfer factor, j, is useful to investigate a wide range of forced convection problems with different combinations of Re and Pr.[21,22,31,39] We define a similar factor for the mixed convection flow within the steady laminar regime. This new factor j_{Ri} is defined as

$$j_{Ri} = \frac{Nu_{avg}Ri}{Re^{0.44}Pr^{0.346}}. \tag{13}$$

The exponents in Equation (13) are obtained by curve fitting of the data from all the computations we performed in the range $10 \leq Re \leq 35$; $0.05 \leq Ri \leq 2$; $0.25 \leq Pr \leq 100$. For comparison, we also define

$$j_v = \frac{Nu_{avg}Ri}{Re^{0.32}Pr^{0.31}}, \tag{14}$$

which is motivated by the correlation $Nu_{avg} = 1.34Pr^{0.31}Re^{0.32}$ given by the experimental studies of Ref. 16 in the range $Ri \leq 0.5$.

The factor j_v is plotted against Ri for various combinations of Re and Pr in Figure 5(a). The plot suggests that the correlation of Vilimpoq *et al.*[16] is reasonably valid in the range $Ri \leq 0.5$ though the data exhibit notable deviations from the correlation for Ri close to 0.5. More importantly,
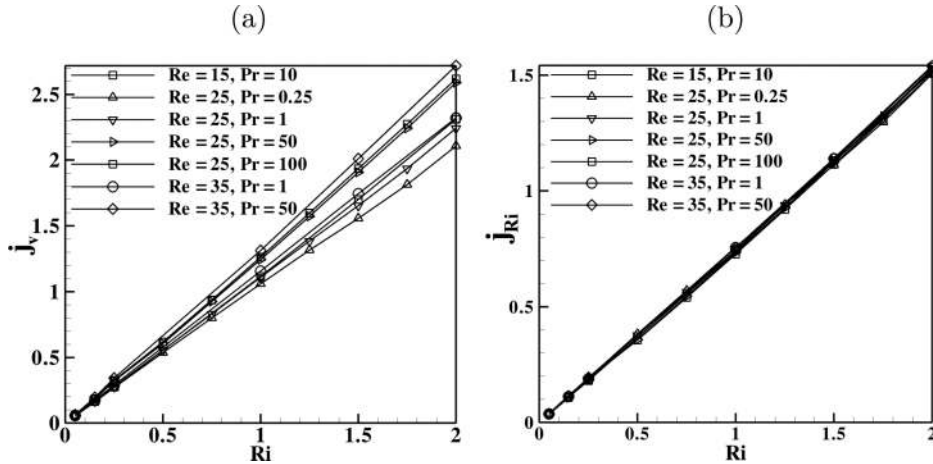
FIG. 5. Variation of (a) j_v (Equation (14)) and (b) j_{Ri} (Equation (13)) with Ri for various values of Re and Pr. The best fit straight line in (b) is given by $j_{Ri} = 0.7435Ri$.

the deviations of our data from the expression for Nu_{avg} given by Ref. 16 are significant for Ri larger than 0.5. The factor j_{Ri} is plotted against Ri for all the combinations of Re and Pr in Figure 5(b). As observed for $Re = 25$ in Figure 4, an increase in Pr increases Nu_{avg} for other Reynolds numbers as well. The exponent value of 0.346 for Pr in Equation (13) (which incorporates data from various Re) differs a little from the exponent of 1/3 obtained using the $Re = 25$ data only.

The linear variation of j_{Ri} with Ri shown in Figure 5(b) suggests that Nu_{avg} is weakly affected by changes in Ri in the mixed convection regime of the flow past a circular cylinder. It is interesting to note that all the straight line plots in Figure 5(b) obtained for different combinations of Re and Pr fall on one another with a maximum deviation of less than 2%. The factor j_{Ri} thus provides a new, accurate quantification of forced and mixed convection heat transfer (in terms of Nu_{avg}) to a wider range of Re, Pr, and Ri within the laminar separated flow regime. The average Nusselt number is therefore given by

$$Nu_{avg} = 0.7435Re^{0.44}Pr^{0.346}, 10 \leq Re \leq 35, 0.05 \leq Ri \leq 2, 0.25 \leq Pr \leq 100. \qquad (15)$$

B. Effects of Prandtl number on the wake structure behind the cylinder

The flow past an unheated circular cylinder ($\Delta T_d = 0$) in the low Reynolds number regime ($6 < Re < 47$) results in a steady wake region behind the cylinder consisting of a pair of counter-rotating vortices attached to the cylinder.[6] The steady recirculation bubble, consisting of the two counter-rotating vortices that elongate as Re is increased, remains symmetric about the horizontal line passing through the centre of the cylinder, as shown in Figure 6(a), which is plotted for $Re = 25$, $Ri = 0$, and $Pr = 0.25$. We recall that, for $Ri = 0$, the velocity field is independent of Pr and is the same as that for $\Delta T_d = 0$, whereas the temperature field is strongly dependent on Pr.

To investigate the changes induced by introducing buoyancy, we plot the streamlines for $Re = 25, Ri = 0.25$, and $Pr = 0.25$ in Figure 6(b). Unlike the scenario for $Ri = 0$ shown in Figure 6(a), the recirculation bubble in Figure 6(b) is not symmetric about the x-axis. For $Ri = 0.25$ and $Pr = 0.25$, the clockwise and anti-clockwise vortices have moved downstream and upstream, respectively, from their locations for $Ri = 0$. The front stagnation point shifts from 180° for $Ri = 0$°–172° for $Ri = 0.25$ and $Pr = 0.25$. The changes in the flow pattern with variations in Ri and Pr are explained in more detail using Figure 7.

Instantaneous streamlines for a representative Reynolds number of $Re = 25$, which corresponds to a steady recirculation zone for $Ri = 0$, are shown in Figure 7. In Figure 7, Pr varies from 0.25 in the top row to 100 in the bottom row whereas Ri is 0.25, 1.25, and 1.75 in the left, middle, and right columns, respectively. For $Pr = 0.25$, (Figures 7(a)–7(c)), there is a strong loss in symmetry (about the x-axis) as Ri is increased, with strongly skewed vortices observed in the separation bubble for
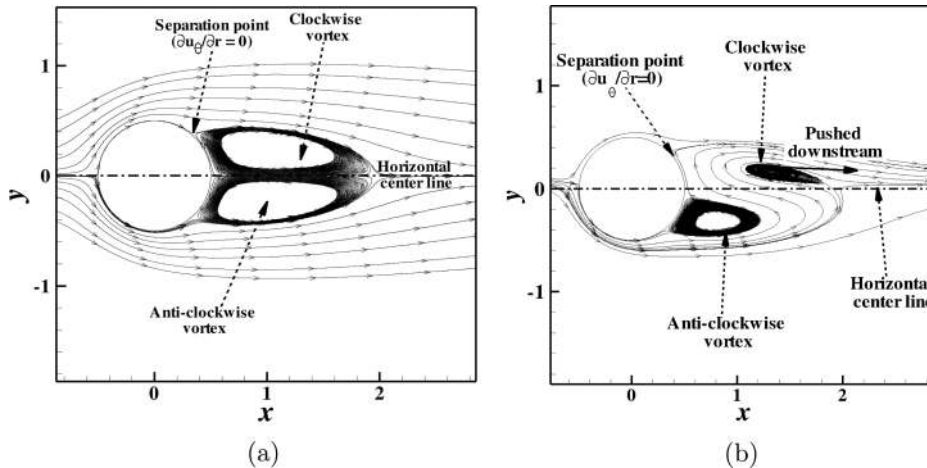
FIG. 6.   Streamlines for $Re = 25$, $Pr = 0.25$ and (a) $Ri = 0.0$, (b) $Ri = 0.25$.

$Ri = 1.25$ and $Ri = 1.75$. The clockwise vortex in the top part of the separation bubble is detached from the cylinder for $Ri = 0.25$, and then continues to move downstream and get elongated in the x-direction as Ri is increased to larger values. The anti-clockwise vortex in the bottom part of the separation bubble, however, remains attached to the cylinder for all Ri but decreases dramatically in size as Ri is increased. The same qualitative changes are observed in the flow pattern with an increase in Ri for $Pr = 1$ and $Pr = 10$, but with the vortices completely disappearing for $Ri = 1.25$, $Pr = 10$ (Figure 7(h)). Based on the results for $Pr = 0.25$, 1, and 10, we conclude that the value of Ri at which the vortices disappear is smaller for larger Pr.

In Figure 7, a part of the mean flow is clearly seen to flow between the top and bottom vortices (Figures 7(a) and 7(d), for example). For $Ri = 0$, there is no flow between the counter rotating vortices in the recirculation bubble. A part of the free stream flow entering between the two vortices is seen in this context as inducing an extra clockwise spin to the detached vortex, creating a movement downstream. At high Ri, the net buoyancy force is larger and the flow around the cylinder tends to move upwards. The resultant of this upward velocity and the mean flow velocity disturbs the symmetry in such a way that the upper vortex is pushed further downstream, while the lower is reduced in size. At sufficiently high Ri, the recirculation bubble extinguishes completely, with the disappearance of both the bottom and top vortices, as seen in Figure 7(h).

For $Pr = 50$, as shown in the Figures 7(j)-7(l), increasing Ri after the disappearance of the two vortices results in the regeneration of the clockwise top vortex; the regeneration is faintly seen in Figure 7(k), and more clearly visible in Figure 7(l). The various stages leading to the disappearance of vortices seem to occur between $Ri = 0.25$ and $Ri = 1.25$ for $Pr = 100$, with the reemergence of the top vortex clearly observed at $Ri = 1.25$ itself (Figures 7(m)-7(o)).

Figures 7(b), 7(e), 7(h), 7(k), and 7(n) show the streamlines in and around the recirculation bubble for $Pr = 0.25, 1, 10, 50$, and 100, respectively with $Re = 25$ and $Ri = 1.25$. As Pr is increased, we observe the disappearance of the skewed vortices that are seen at $Pr = 0.25$, followed by the reemergence of the top vortex at large Pr. Increasing Pr even further to $Pr = 1000$, we observe the reappearance of the bottom vortex also, as shown in Figure 8. In summary, the asymmetric flow field created due to buoyancy seems to be brought back to a symmetric time-averaged flow field by increasing Pr to large enough values, an aspect we proceed to investigate further in detail.

As confirmed by the more crowded isotherms around the cylinder for larger Pr in Figure 3, the thermal boundary layer thickness decreases with an increase in Pr. In the limit of large Pr, strong temperature gradients are restricted to a very thin thermal boundary layer around the cylinder. We recall that the boundary condition at the cylinder surface is always isothermal with $T = 1$ as discussed in Section II. To investigate the effects of increasing Pr on the near-wake velocity field, in Figure 9, the time-averaged horizontal velocity component u at locations $x = 1$ and $x = 2$ (marked
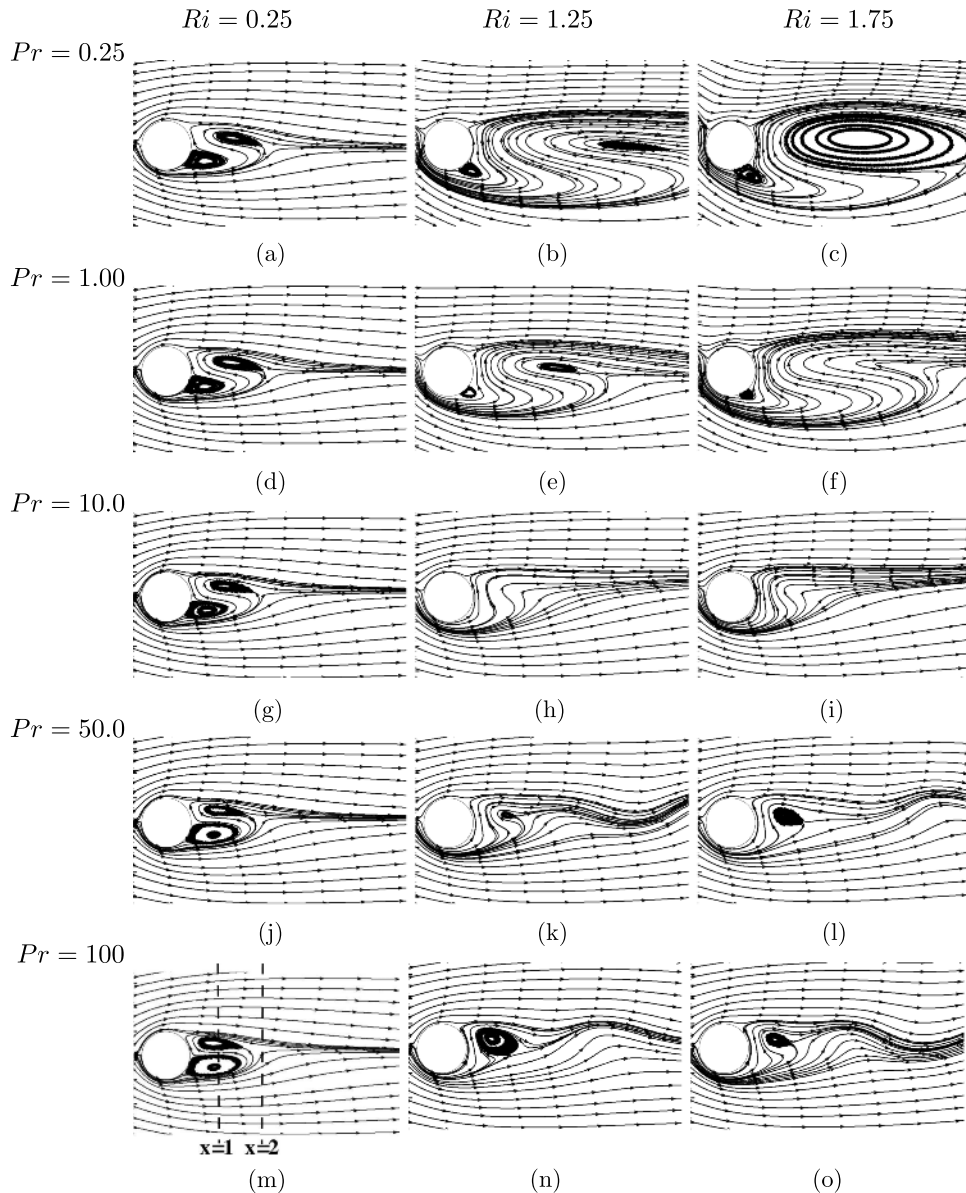
FIG. 7. Instantaneous streamlines for $Re = 25$ and various combinations of Ri and Pr. The two vertical dashed lines in the plot for $Ri = 0.25$ and $Pr = 100$ correspond to the locations at which velocity profiles are plotted in Figure 9.

as dotted lines in Figure 7(m)) is plotted against the vertical coordinate y for various Pr at $Re = 25$ and $Ri = 2$. The time-averaged velocity profiles at these two different locations tend to converge to the $Ri = 0$ profile (and hence regain symmetry) at large Pr.

Upon further investigation of the $Re = 25$, $Ri = 1.25$ case, we observed that the pressure field on the cylinder surface does not converge to the $Ri = 0$ case as $Pr \to \infty$. Specifically, at $Pr = 10^3$, we find the pressure and pressure gradients on the cylinder to be notably different from those at $Ri = 0$, thus suggesting that while the symmetry about the centerline is regained as $Pr \to \infty$, the flow field does not exactly converge to the $Ri = 0$ scenario. We recall that an increase in Pr makes the energy equation (4) convection-dominant, whereas an increase in Ri strengthens the coupling between the momentum and energy equations. Therefore, a simultaneous increase of Ri and Pr is intuitively expected to increase the likelihood of instabilities and subsequently vortex shedding.
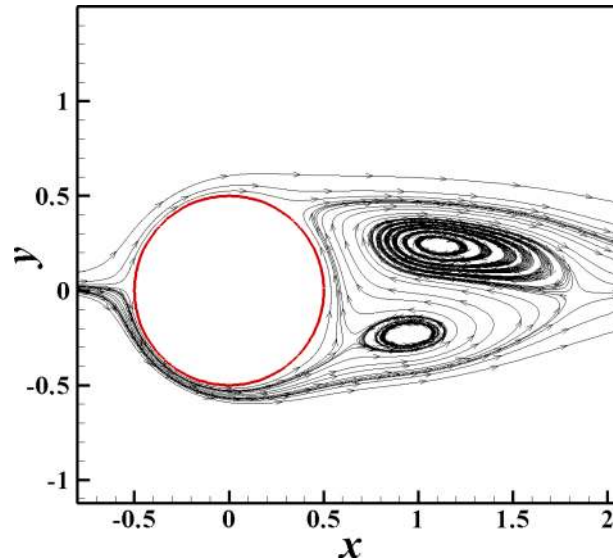
FIG. 8. Instantaneous streamlines for $Re = 25$, $Ri = 1.25$ and $Pr = 1000$. The reappearance of the anticlockwise vortex below the x-axis for large Pr is consistent with our conjecture that time-averaged near-wake region behind the cylinder tends to regain symmetry as $Pr \to \infty$.

An outstanding feature of the flow fields at relatively large values of Ri and Pr is their unsteadiness in regions far from the cylinder, in Figures 7(l) and 7(o) for example. Plotting the streamlines as a function of time for $Ri = 1.75$, $Pr = 100$, we find that the streamlines far from the cylinder oscillate in time, and the vortex near the cylinder shrinks and enlarges periodically. To investigate whether vortex shedding occurs in these unsteady scenarios, we plot snapshots of the vorticity field in Figure 10. For $Ri = 1.25$, while the vorticity fields for $Pr = 0.25$ and $Pr = 1$ show continuously varying asymmetric patches of positive and negative vorticities, at $Pr = 5$ we observe a series of isolated patches of negative vorticity in the upper half-plane. Indeed, plotting the vorticity field as a function of time for $Ri = 1.25$, $Pr = 5$ shows vortex shedding-like features, but with the shedding initiated far from the cylinder and seemingly only in the upper half-plane. As Pr is increased further, as shown in Figures 10(g) and 10(i), the vortex shedding becomes more distinct, with the upward deflection of the vortex street being reduced. Finally, at large Pr, as shown in Figures 10(k) and
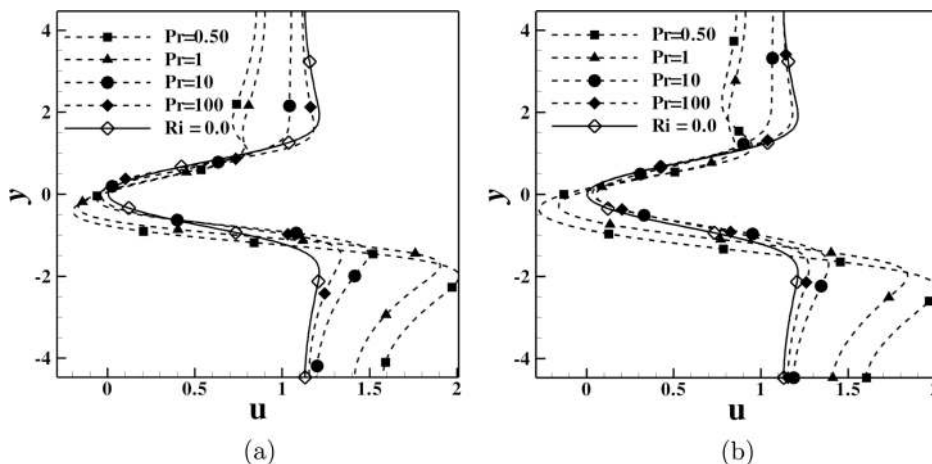
FIG. 9. Time-averaged horizontal velocity profiles at locations (a) $x = 1$ and (b) $x = 2$ (indicated in Figure 7(m)) for $Re = 25$, $Ri = 2$, and various Pr. The solid curve corresponds to the unheated case at $Re = 25$. The profiles for $Ri = 2$ tend towards the profile at $Ri = 0$ as Pr is increased.
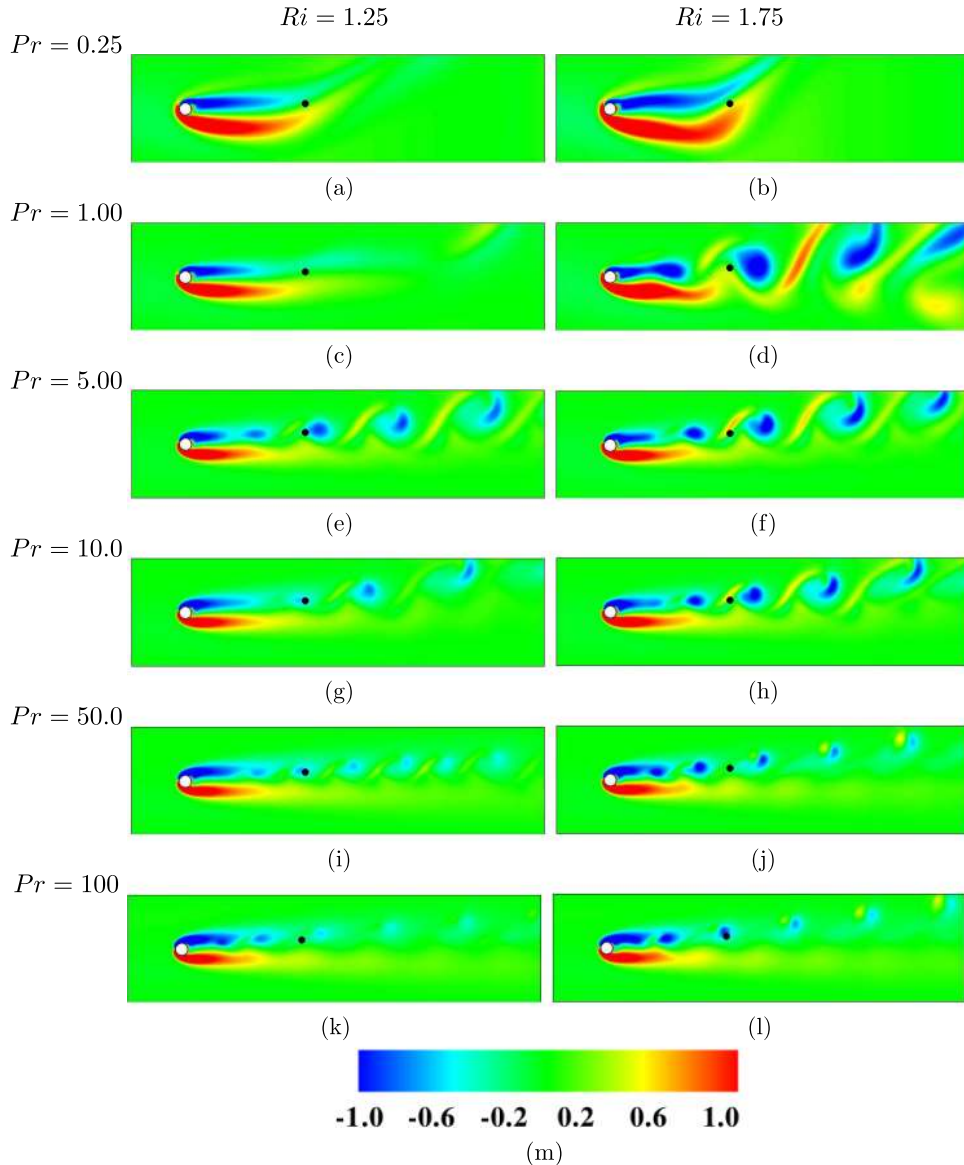
FIG. 10. Snapshots of vorticity field for $Re = 25$ and various combinations of Ri and Pr. The black dots in each of the figures indicate the spatial locations at which corresponding time series are plotted in Figure 11.

10(m), the vortex shedding is suppressed, with the flow field regaining symmetry about the centre-line. At larger Ri, as shown in the right column of Figure 10, we observe a similar progression of events as Pr is increased, but with a smaller Pr at which vortex shedding is initiated, and a larger Pr at which it is seemingly suppressed.

To probe the nature of the flow unsteadiness far from the cylinder, we plot (in Figure 11) representative time series of u for all the cases shown in Figure 10. The spatial locations, specifically chosen to be in regions where vortex shedding occurs, corresponding to the various time series are indicated by black dots in Figure 10. For $Ri = 1.25$, as shown in the left column of Figure 11, the flow is steady at $Pr = 0.25$, then becomes unsteady with a near-sinusoidal behaviour at $Pr = 1$, and progressively becomes more non-sinusoidal with an increase in Pr. For all Pr except $Pr = 0.25$, we observe the presence of a dominant frequency in the power spectra, and higher harmonics (integer multiples of the dominant frequency) that become relatively stronger as Pr is increased. A qualitatively similar evolution of the time series (and power spectra) with Pr is observed for $Ri = 1.75$, but
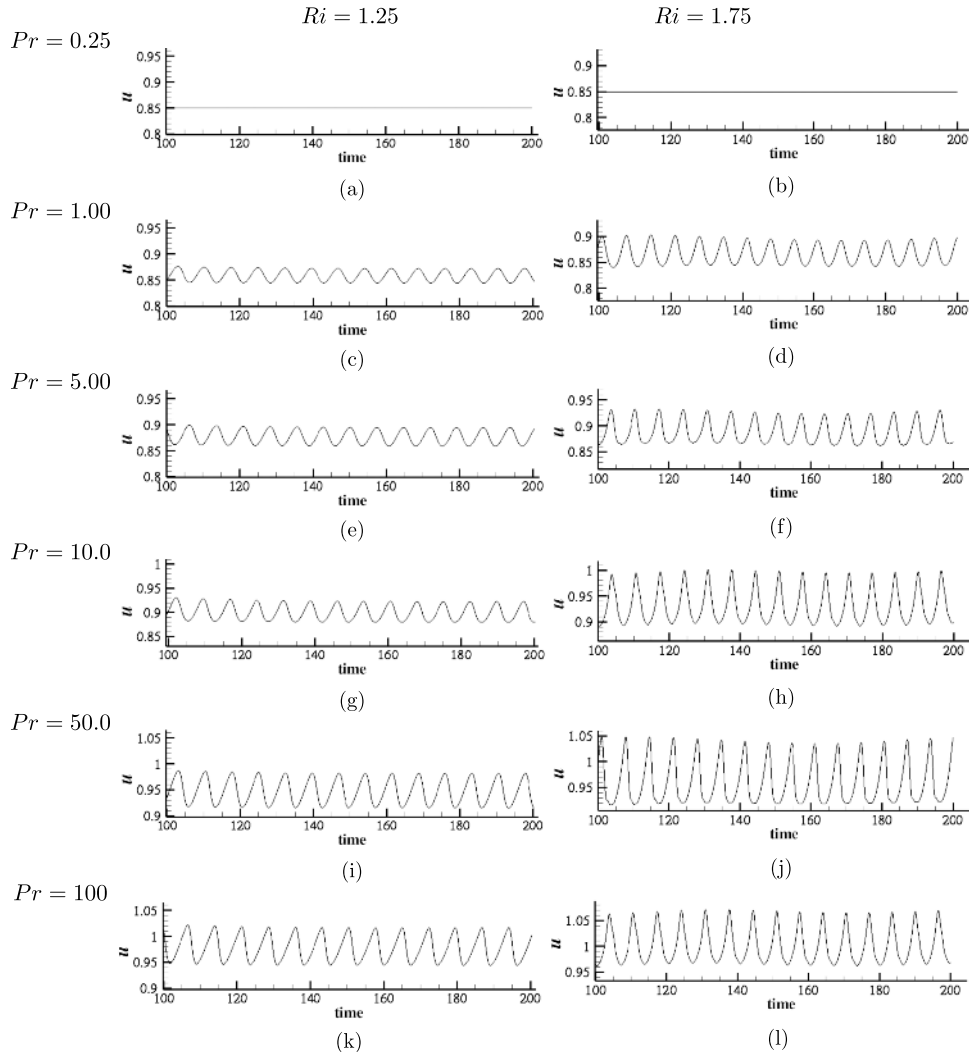
FIG. 11. Time series of u at specific spatial locations (indicated by the black dots in Figure 10) for all the cases shown in Figure 10.

with noticeably larger energy in a continuous range of frequencies between the dominant frequency and the second harmonic (twice the dominant frequency).

More importantly, the flow in a close neighbourhood of the cylinder surface remains steady for all practical purposes, allowing us to compute a single value for quantities such as Nu, C_L, C_D, the stagnation, separation, and plume generation locations for every case. As an example, in Figure 12(a) we have plotted the variation of C_L and C_D with time for two different cases: $Re = 25$, $Ri = 1.75$ with (i) $Pr = 0.25$, (ii) $Pr = 100$, both of which show unsteadiness in the streamlines far from the cylinder. As confirmed by Figure 12(a), the wall-based quantities indeed attain a steady state value despite the far-field flow being unsteady. Specifically, the rms of the fluctuations in C_L and C_D for the two cases shown in Figure 12(a) is of the order of 10^{-6}.

The front stagnation angle θ_S, defined as the azimuthal coordinate of the front stagnation point, is an important feature of the flow pattern around the cylinder. As shown in Figure 12(b), θ_S decreases with Ri and increases with Pr, with a relatively weak dependence on Re. The asymmetric streamline pattern for $Ri > 0$ thus contains more streamlines below the dividing streamline if we start with an equispaced set of streamlines at the inlet of the computational domain where the velocity is constant. For example, at $Ri = 1$ (Figure 13(c)), the stagnation point is at 172° and results in a larger volume of fluid passing below the cylinder than for $Ri = 0$ (Figure 13(a)). Apart from our
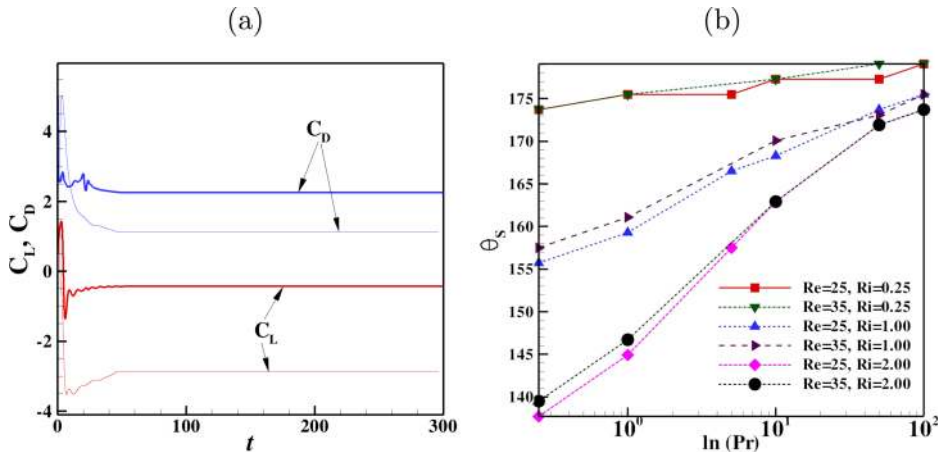
FIG. 12. (a) Lift and drag coefficients (C_L and C_D) plotted as a function of time for $Re = 25, Ri = 1.75, Pr = 0.25$ (thin line) and $Re = 25, Ri = 1.75, Pr = 100$ (thick line). (b) Variation of the front stagnation angle with Pr for different combinations of Re and Ri. Note that the stagnation angle remains constant with time for all the cases.

earlier inference of the flow pattern in the near-wake region regaining symmetry at large Pr for all Ri, θ_S also converges to $\theta_S = 180°$ at large Pr for all Ri.

C. Effects of Prandtl number on the thermal plume structure

Hot fluid rising due to buoyancy is often termed a plume, even though a clear definition of a "plume" is still lacking.[40–42] Thermal plumes, which typically occur due to boundary layer instability in thermal convection flows,[43] are relevant for understanding the distribution of heat transfer in flows with a spatially varying temperature field. The plume locations are identified by a spike or carbuncle-like feature in the temperature contours near the cylinder surface. The carbuncles, i.e., bulges in the isotherms as seen in Figures 13(c) and 13(d), are locations of small $\partial T/\partial r$, thus allowing us to identify plume generation locations as local minima of the Nusselt number Nu_θ on the cylinder surface. We recall that the temperature on the cylinder surface is held constant at $T = 1$. In other words, the generation of plumes occur at the points on the cylinder where $\partial Nu_\theta/\partial\theta = 0$ and $\partial^2 Nu_\theta/\partial\theta^2 > 0$. In this section, via temperature contour and streamline plots, we discuss the variation of the thermal plume generation and viscous boundary layer separation points as a function of Pr.

Figure 13 shows the isotherms and the dividing streamline for four different combinations of Ri and Pr at $Re = 30$. At zero buoyancy ($Ri = 0$), for which temperature is a passive scalar, there are no plumes. As shown in Figures 13(a) and 13(b), carbuncles are nevertheless present in the isotherms for $Ri = 0$ and are aligned with the dividing streamline along which flow separation occurs. The locations of flow separation are identified as the points on the cylinder that satisfy $\partial u_\theta/\partial r = 0$. The carbuncle locations in the isotherms for $Ri = 0$ are therefore symmetric about the horizontal center line of the cylinder and are independent of the value of Pr. The Reynolds number, however, affects the flow separation points at $Ri = 0$.[6]

In the presence of buoyancy, i.e., $Ri > 0$, the flow is not symmetric about the horizontal center line, and the temperature field is no longer a passive scalar. For the rest of this section, we focus on the dynamics of the flow occurring in the upper half-plane $y > 0$. As shown in Figures 13(c) and 13(d), the plumes, identified by the carbuncles in the isotherms, rise vertically upwards at the cylinder surface. The rising plume is then driven along the streamwise direction by the mean wind/free stream. For $Pr = 1$, as shown in Figure 13(c), we observe a noticeable difference between the plume locations and the dividing streamline. At $Pr = 100$, however, the plume is generated near the flow separation point and grows along the dividing streamline. It may be noted that the flow separation point changes only marginally with Pr, as shown in Figure 15(a).
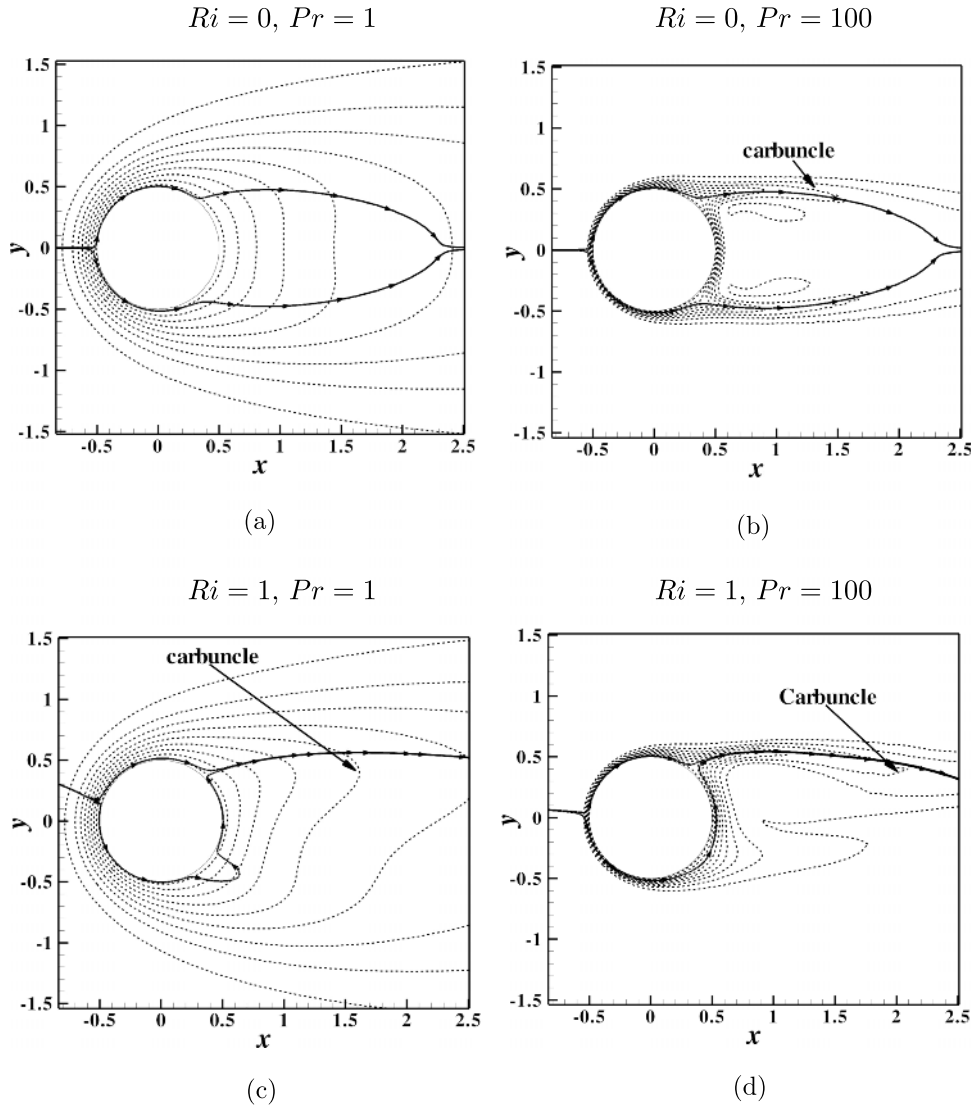
FIG. 13. Instantaneous isotherms and dividing streamline for $Re = 30$. The top and bottom rows correspond to $Ri = 0$ and $Ri = 1$, respectively. The left and right columns correspond to $Pr = 1$ and $Pr = 100$, respectively. The solid lines indicate the dividing streamlines and the dotted lines indicate the isotherms around the cylinder. The isotherms in all the four figures correspond to the same set of values of T.

The asymptotic behavior of the flow field at large Pr for all Ri is further investigated by plotting the variation of the flow separation and the plume generation angles with Pr. We define α_{sep} and α_{plume} as the azimuthal coordinate of the points on the cylinder where flow separation and plume generation, respectively, occur. The difference between the flow separation and the plume generation locations is then quantified by $\alpha = \alpha_{sep} - \alpha_{plume}$. The various geometric features of the flow pattern and the isotherms are depicted in Figure 14.

Figure 14 shows a zoomed-in region near the separation point for $Re = 35$, $Ri = 1$, and $Pr = 1$. The flow separation and plume generation points on the cylinder surface are shown. In Figures 15(a) and 15(b), the angles α_{sep} and α_{plume} are plotted for four different pairs of (Re, Ri), with Pr varying from 0.25 to 100 for each pair. The difference between the separation and plume locations reduces if the Prandtl number increases and is consolidated in Figure 15(c). In Figure 15(c), the difference $\alpha = \alpha_{sep} - \alpha_{plume}$ is plotted as a function of Pr for different combinations of Re and Ri. While both α_{sep} and α_{plume} increase with an increase in Pr, the difference approaches zero as Pr increases.
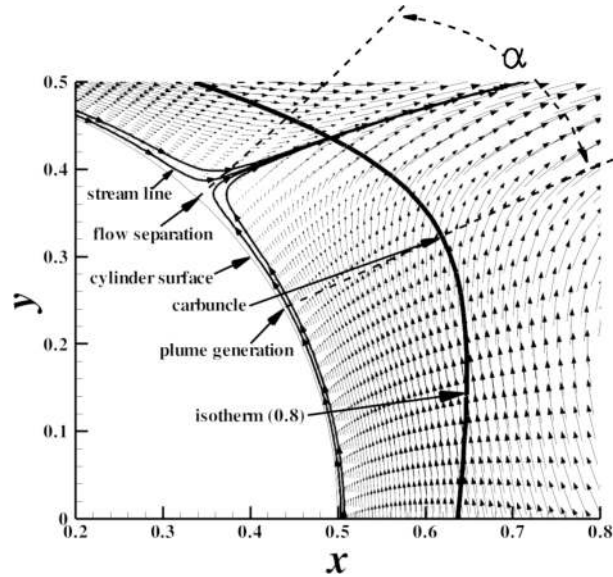
FIG. 14. Flow field near the separation point for $Re = 35$, $Ri = 1.0$, and $Pr = 1.0$. The separation point and the plume generation point are different, with the angle between the two points shown as α in the plot.

D. Effects of Prandtl number on force coefficients—C_L and C_D

As discussed in Section III B, the front stagnation point moves to the upper half of the cylinder for $Ri > 0$, with the resulting flow pattern suggestive of a net lift force in the negative y-direction. In Figure 16(a), we plot the lift coefficient C_L (Equation (9)) as a function of Ri for various Pr at $Re = 25$. The magnitude of C_L increases with Ri, with a stronger rate of increase for small Pr. Correspondingly, we plot C_L as a function of Pr for various Ri at $Re = 25$ in Figure 16(b). For all Ri, the magnitude of C_L decreases with Pr and asymptotically converges to zero at large Pr. We recall that the symmetric flow field associated with $Ri = 0$ corresponds to $C_L = 0$ too.

In Figure 17(a), the variation of the drag coefficient C_D (Equation (10)) with Ri is plotted for various Pr and $Re = 25$. For small Pr (less than around 7.5), C_D decreases with Ri, reaching values close to 50% of $C_D|_{Ri=0}$ at $Ri = 2$ and $Pr = 0.25$. Interestingly, the change in C_D with Ri is very small at $Pr = 7.5$, which is close to the value of Pr for water at standard conditions. For $Pr > 7.5$, however, we observe an increase in C_D with Ri, implying that drag reduction upon heating the cylinder occurs only for small enough values of Pr. Figure 17(b) shows the variation of C_D with Pr for various Ri and $Re = 25$. It is observed that for all the values of Ri, C_D increases with Pr and reaches a nearly constant value at large Pr. The asymptotic value of C_D at large Pr, however, depends on Ri. The stress distribution on the cylinder surface therefore does not converge to the case of $Ri = 0$ in the limit of large Pr for any $Ri > 0$.
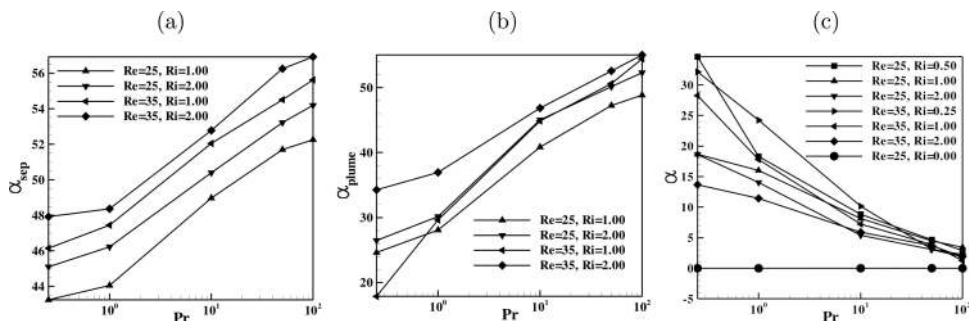
FIG. 15. Variation of (a) α_{sep}, (b) α_{plume}, and (c) $\alpha = \alpha_{sep} - \alpha_{plume}$ (in degrees) with Pr for different combinations of Re and Ri.
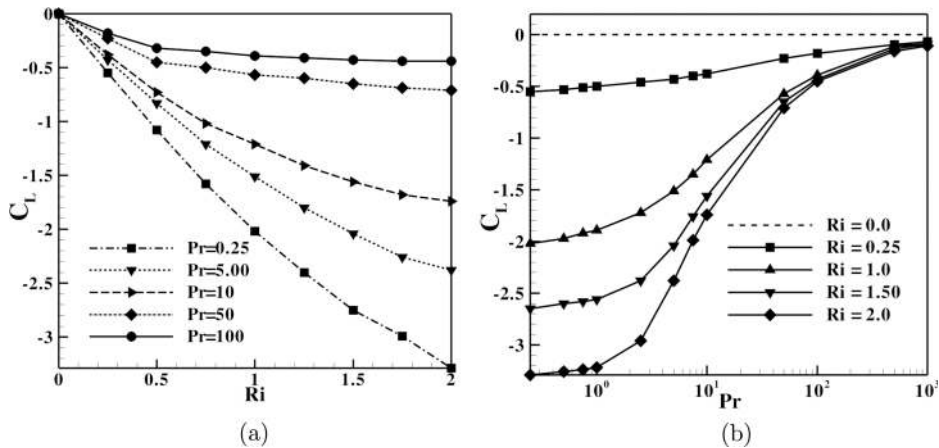
FIG. 16. (a) Variation of C_L with Ri for different values of Pr at $Re = 25$. (b) C_L variation with Pr for various Ri. As Pr increases C_L approaches zero.
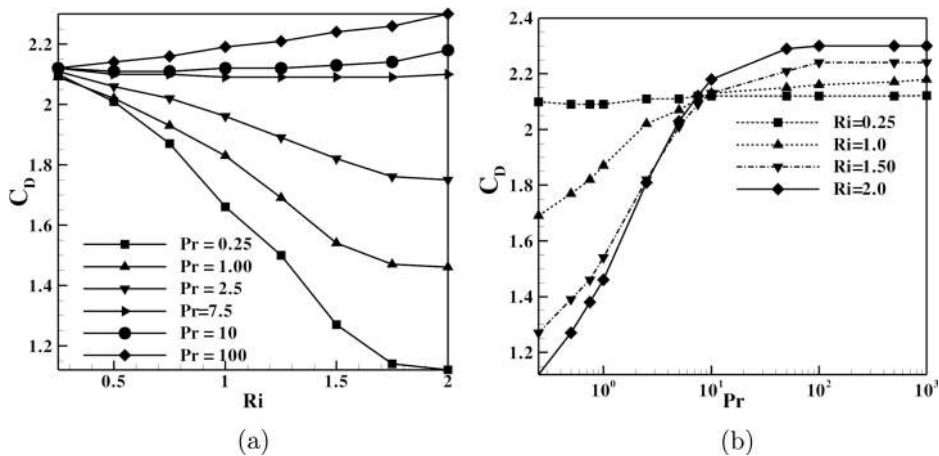
FIG. 17. (a) Variation of C_D with Ri for different values of Pr at $Re = 25$. (b) Variation of C_D with Pr for different Ri.

IV. CONCLUSIONS

In this paper, we have performed a numerical study of the role of Prandtl number in the flow past a heated cylinder in the mixed convection regime. Specifically, we have presented a detailed analysis of the laminar flow in the parameter range specified by $Re \leq 35$, $0 \leq Ri \leq 2$, and $0.25 \leq Pr \leq 10^2$, including some results for $Pr = 1000$ wherever necessary.

The Nusselt number Nu_θ and the average Nusselt number Nu_{avg}, which is a measure of the heat transfer from the entire cylinder surface, increase with an increase in Pr. The variation of Nu_{avg} with Re, Ri, and Pr is well captured by the relation: $Nu_{avg} = 0.7435Re^{0.44}Pr^{0.346}$, valid for $10 \leq Re \leq 35$, $0.05 \leq Ri \leq 2$, $0.25 \leq Pr \leq 100$. This relation represents a significant improvement over what exists in the current literature.[16] The isotherms plotted around the cylinder are asymmetric about the centerline for $Ri > 0$, and contain spikes/carbuncles along which thermal plumes are presumed to grow. The locus of the carbuncles is traced back to the minimum Nu_θ point on the cylinder surface, identified as the plume generation location.

The asymmetry about the centerline for $Ri > 0$ is also observed in the streamline and vorticity plots, with the vortices in the recirculation bubble getting distorted as Ri is increased from zero. As Ri is increased, the top vortex gets pushed downstream whereas the bottom vortex, which reduces in size, gets closer to the cylinder. Upon reaching a threshold Ri, both the vortices in the recirculation bubble disappear, followed by the reappearance of the top vortex at a larger Ri. A similar behaviour

is observed with an increase in *Pr* for a fixed *Re* and *Ri*, but with the reappearance of both the vortices beyond a threshold value of *Pr*.

The near-wake flow field regains symmetry about the centerline in the limit of large *Pr*. This observation is substantiated with time-averaged velocity profile plots (*u* vs. *y* at two different streamwise locations) that almost regain symmetry at *Pr* = 100 for *Ri* = 2. For a fixed *Re* and *Ri*, asymmetric vortex shedding is seen to be initiated far from the cylinder above some threshold value of *Pr*; as *Pr* is increased further, the upward deflection of the shed vortices decreases, and the vortex shedding is seemingly suppressed at very large *Pr* giving way to a symmetric flow field. The location of the front stagnation point converges to the *Ri* = 0 case at large *Pr*, with the front stagnation angle approaching $\theta_S = 180°$ from a smaller value as *Pr* is increased to large values for a fixed *Re* and *Ri*. The difference between the flow separation and plume generation locations, quantified by the quantity α, was studied in Section III C with the main conclusion that α can be as large as 30° at small *Pr* but converges to zero at large *Pr*.

The variation of the time-averaged lift and drag coefficients, C_L and C_D, with *Ri* and *Pr* for *Re* = 25 was investigated in Section III D. C_L is negative for *Ri* > 0, and its magnitude increases with *Ri* for a fixed *Pr*. For all *Ri*, the magnitude of C_L decreases with *Pr*, converging to $C_L = 0$ at large *Pr*. C_D is observed to decrease with *Ri* for small enough *Pr*, whereas C_D increases with *Ri* at larger *Pr*. Values of *Re* and *Ri* outside the ranges considered here would result in three dimensional effects, which are not discussed in the present paper.

ACKNOWLEDGMENTS

[1] S. Taneda, "Experimental investigation of the wakes behind cylinders and plates at low Reynolds numbers," J. Phys. Soc. Jpn. **11**, 302 (1956).

[2] J. H. Gerrard, "The mechanics of the formation region of vortices behind bluff bodies," J. Fluid Mech. **25**, 401–413 (1966).

[3] S. C. R. Dennis and G. Z. Chang, "Numerical solutions for steady flow past a circular cylinder at Reynolds numbers up to 100," J. Fluid Mech. **42**, 471–489 (1970).

[4] C. H. K. Williamson and A. Roshko, "Measurements of base pressure in the wake of a cylinder at low Reynolds numbers," Z. Flugwiss. Weltraumforsch. **14**, 38–46 (1990).

[5] A. Roshko, "Perspectives on bluff body aerodynamics," J. Wind Eng. Ind. Aerodyn. **49**, 79–100 (1993).

[6] M. M. Zdravkovich, *Flow Around Circular Cylinders: Fundamentals* (Oxford University Press, New York, 1997), Vol. 1.

[7] S. Sen, S. Mittal, and G. Biswas, "Steady separated flow past a circular cylinder at low Reynolds number," J. Fluid Mech. **620**, 89–119 (2009).

[8] D. C. Collis and M. J. Williams, "Two-dimensional convection from heated wires at low Reynolds numbers," J. Fluid Mech. **6**, 357–384 (1959).

[9] H. Jafroudi and H. T. Yang, "Steady laminar forced convection from a circular cylinder," J. Comput. Phys. **65**, 46–56 (1986).

[10] S. C. R. Dennis, J. D. Hudson, and N. Smith, "Steady laminar forced convection from a circular cylinder at low reynolds numbers," Phys. Fluids **11**, 933–940 (1968).

[11] A. K. Sahu, R. P. Chhabra, and V. Eswaran, "Effects of Reynolds and Prandtl numbers on heat transfer from a square cylinder in the unsteady flow regime," Int. J. Heat Mass Transfer **52**, 839–850 (2009).

[12] B. Gebhart, L. Pera, and A. W. Schorr, "Steady laminar natural convection plumes above a horizontal line heat source," Int. J. Heat Mass Transfer **13**, 161–171 (1970).

[13] B. Gebhart and L. Pera, "Mixed convection from long horizontal cylinders," J. Fluid Mech. **45**, 49–64 (1970).

[14] P. H. Oosthuizen and S. Madan, "The effect of flow direction on combined convective heat transfer from cylinders to air," J. Heat Transfer **93**(2), 240 (1971).

[15] R. M. Fand and K. K. Keswani, "Combined natural and forecd convection heat transfer from horizontal cylinders to water," Int. J. Heat Mass Transfer **16**, 1175–1191 (1973).

[16] V. Vilimpoq, R. Cole, and P. C. Sukanek, "Heat transfer in newtonian liquids around a circular cylinder," Int. J. Heat Mass Transfer **33**, 447–456 (1990).

[17] J. C. Lecordier, L. W. B. Browne, S. Le Masson, F. Dumouchel, and P. Paranthoen, "Control of vortex shedding by thermal effect at low Reynolds numbers," Exp. Therm. Fluid Sci. **21**, 227–237 (2000).

[18] A. A. van Steenhoven and C. C. M. Rindt, "Flow transition behind a heated cylinder," Int. J. Heat Fluid Flow **24**, 322–333 (2003).

[19] R. N. Kieft, C. C. M. Rindt, A. A. van Steenhoven, and G. J. F. van Heijst, "On the wake structure behind a heated horizontal cylinder in cross-flow," J. Fluid Mech. **486**, 189–211 (2002).

[20] C. K. Lee and P. D. Richardson, "Forced convection from a cylinder at moderate reynolds numbers," Int. J. Heat Mass Transfer **17**, 609–613 (1973).

[21] S. Sanitjai and R. J. Goldstein, "Forced convection heat transfer from a circular cylinder in crossflow to air and liquids," Int. J. Heat Mass Transfer **47**, 4795–4805 (2004).

[22] S. Sanitjai and R. J. Goldstein, "Heat transfer from a circular cylinder to mixtures of water and ethylene glycol," Int. J. Heat Mass Transfer **47**, 4785–4794 (2004).

[23] A. Acrivos, D. D. Snowden, A. S. Grove, and E. E. Petersen, "The steady separated flow past a circular cylinder at large Reynolds number," J. Fluid Mech. **21**(4), 737–760 (1965).

[24] S. Lee, K. Wong, and C. Chen, "The finite element solution of laminar combined convection from a horizontal cylinder," Comput. Methods Appl. Mech. Eng. **50**, 147–161 (1985).

[25] F. Dumouchel, J. C. Lecordier, and P. Paranthoen, "The effective Reynolds number of a heated cylinder," Int. J. Heat Mass Transfer **41**, 1787–1794 (1998).

[26] C. F. Lange, F. Durst, and M. Breuer, "Momentum and heat transfer from cylinders in laminar cross flow at $10^{-4} \leq Re \leq 200$," Int. J. Heat Mass Transfer **41**, 3409–3430 (1998).

[27] A. B. Wang, Z. Travnicek, and K. Chia, "On the relationship of effective reynolds number and strouhal number for the laminar vortex shedding of a heated circular cylinder," Phys. Fluids **12**, 1401–1410 (2000).

[28] A. B. Wang and Z. Travnicek, "On the linear heat transfer correlation of a heated circular cylinder in laminar cross ow using a new representative temperature concept," Int. J. Heat Mass Transfer **44**, 4635–4647 (2001).

[29] J. M. Shi, D. Gerlach, M. Breuer, G. Biswas, and F. Durst, "Heating effect on steady and unsteady horizontal laminar flow of air past a circular cylinder," Phys. Fluids **16**, 4331–4345 (2004).

[30] M. Wu, C. Wen, R. Yen, M. Weng, and A. B. Wang, "Experimental and numerical study of the separation angle for flow around a circular cylinder at low reynolds number," J. Fluid Mech. **515**, 233–260 (2004).

[31] R. P. Bharti, R. P. Chhabra, and V. Eswaran, "A numerical study of the steady forced convection heat transfer from an unconfined circular cylinder," Heat Mass Transfer **43**, 639–648 (2007).

[32] G. Biswas and S. Sarkar, "Effect of thermal buoyancy on vortex shedding past a circular cylinder in cross-flow at low Reynolds numbers," Int. J. Heat Mass Transfer **52**, 1897–1912 (2009).

[33] J. Guermond, P. Minev, and J. Shen, "An overview of projection methods for incompressible flows," Comput. Methods Appl. Mech. Eng. **195**, 6011–6045 (2006).

[34] S. Anil Lal and E. Jabir, "A hybrid finite element-finite volume method for incompressible flow through complex geometries using mixed grids," Proc. Inst. Mech. Eng., Part G **224**, 23–41 (2009).

[35] R. Verzicco and R. Camussi, "Transitional regimes of low-prandtl thermal convection in a cylindrical cell," Phys. Fluids **9**, 1287–1295 (1997).

[36] E. M. Sparrow, J. P. Abraham, and J. C. K. Tong, "Archival correlations for average heat transfer coefficients for non-circular and circular cylinders and for spheres in cross-flow," Int. J. Heat Mass Transfer **47**, 5285–5296 (2004).

[37] A. A. Soares, J. M. Ferreira, and R. P. Chhabra, "Flow and forced convection heat transfer in crossflow of non-Newtonian fluids over a circular cylinder," Ind. Eng. Chem. Res. **44**, 5815–5827 (2005).

[38] D. Chatterjee, "Triggering vortex-shedding by superimposed thermal buoyancy around bluff obstacles in cross-flow at low reynolds numbers," Numer. Heat Transfer, Part A **61**(10), 800–806 (2012).

[39] A. K. Dhiman, R. P. Chhabra, A. Sharma, and V. Eswaran, "Effects of reynolds and prandtl numbers on heat transfer across a square cylinder in the steady flow regime," Numer. Heat Transfer, Part A **49**, 717–731 (2006).

[40] R. Verzicco and R. Camussi, "Prandtl number effects in convective turbulence," J. Fluid Mech. **383**, 55–73 (1999).

[41] E. Moses, G. Zocchis, and A. Libchaber, "An experimental study of laminar plumes," J. Fluid Mech. **251**, 581–601 (1993).

[42] L. P. Kadanoff, "Turbulent heat flow: Structures and scaling," Phys. Today **54**(8), 34–39 (2001).

[43] E. M. Sparrow, R. B. Husar, and R. J. Goldstein, "Observations and other characteristics of thermals," J. Fluid Mech. **41**, 793–800 (1990).